Journal of Membrane Science 505 (2016) 205–215

Contents lists available at ScienceDirect

Journal of Membrane Science

journal homepage: www.elsevier.com/locate/memsci

# Fouling behavior during microfiltration of silica nanoparticles and polymeric stabilizers

Krzysztof W. Trzaskus, Aneta Zdeb, Wiebe M. de Vos, Antoine Kemperman, Kitty Nijmeijer

*Membrane Science & Technology, MESA+ Institute of Nanotechnology, University of Twente, Faculty of Science and Technology, 7500 AE Enschede, The Netherlands*

ARTICLE INFO

*Article history:*
Received 6 August 2015
Received in revised form
1 December 2015
Accepted 16 January 2016
Available online 21 January 2016

*Keywords:*
Silica nanoparticle
Fouling
Steric stabilization
Microfiltration

ABSTRACT

Nanotechnology applications give rise to new forms of water pollution, resulting in a need for reliable technologies that can remove nanoparticles from water. Membrane filtration is an obvious candidate. The tendency of nanoparticles to become instable in suspension and form aggregates strongly influences their filtration behavior. This experimental study investigated fouling and rejection during dead-end microfiltration of sterically stabilized nanoparticles. Polyvinylpyrrolidone (PVP) with different molecular weights at different concentrations was used as model steric stabilizer. The large difference between membrane pore size (~200 nm) and the size of the silica nanoparticles (25 nm) allowed a detailed investigation of the filtration process and fouling development. We characterized the feed solution with optical reflectometry, dynamic light scattering, zeta potential measurements and asymmetric flow field flow fractionation (AF4) combined with static light scattering. Subsequently, we looked at the influence of the steric stabilizer (PVP) on nanoparticle fouling development during pore blocking and cake filtration stages.

Our work demonstrates that molecular mass, concentration of the steric stabilizer (PVP) and filtration pressure significantly influence pore blockage and cake filtration. Using a stabilizer with a lower molecular mass generally led to better stabilization of the nanoparticles and the stabilizer contributed less to the fouling. While higher concentrations of the stabilizer enhanced the stability of the nanoparticles, they also caused faster fouling development due to the higher total solute load. Stabilizer with a higher molecular mass was found to contribute more to pore blockage and lead to faster fouling development. Use of a higher transmembrane pressure resulted in compression of the filtration cake, resulting in improved nanoparticle rejection at the expense of permeability.



## 1. Introduction

The exponential growth of nanotechnology creates new sources of water pollution because engineered nanoparticles occur in many common products, such as pigments, coatings and cosmetics, nowadays and are eventually released into the aqueous environment [1–3]. Water pollution with nanoparticles is therefore expected to become an increasingly serious problem [4]. Although the number of studies into the effect of nanoparticles on living organisms is still low relative to their wide range of application, most researchers suggest that nanoparticles are toxic [5,6] and that their small size allows easy penetration into organs and cells [7]. Therefore, reliable technologies for nanoparticle removal from water sources are needed.

Membrane technology is effective in the removal of much larger colloidal particles, but not much is known about the filtration of engineered nanoparticles yet [8,9]. Up-to-date the application of membrane technology is limited by fouling [10] causing pore constriction and internal fouling; this usually necessitates the use of sophisticated cleaning procedures [11–13]. Therefore, it is important to determine the mechanisms, factors and parameters that influence nanoparticle fouling in the initial fouling stage to enable the development of filtration strategies that minimize fouling.

Key factor in the development of fouling is the tendency of the nanoparticles to aggregate [14–16]. The stability of aqueous suspensions of nanoparticles depends on the nanoparticles' surface chemistry, the aquatic environment (pH, ionic strength), and on interactions with other compounds present in the solution [17]. Often, steric or electrostatic stabilizers are added to nanoparticle suspensions to keep the nanoparticles dispersed [18]. Steric stabilization is one of the most commonly used and studied forms of stabilization. Steric repulsion occurs after adsorption of a neutral polymer such as polyvinylpyrrolidone or polyethylene oxide onto the nanoparticle surface and prevents aggregation of nanoparticles. Other organic macromolecules, like humic substances, proteins or saccharides, which are present in many water sources, can also act as steric stabilizers [19–21]. As adsorption of such natural macromolecules leads to transformation of the

http://dx.doi.org/10.1016/j.memsci.2016.01.032
0376-7388/

nanoparticles' surface characteristics and the resulting change in aggregation kinetics, it can facilitate their transport through porous media [22].

The interactions in such feed solutions containing macromolecules and nanoparticles are diverse and simple superposition of the individual fouling contributions cannot be used to describe membrane fouling development in such cases [22]. On the one hand, the higher stability due to steric stabilizers reduces near-membrane surface aggregation as a result of concentration polarization of the rejected nanoparticles [23]. This reduced aggregation of nanoparticles facilitates their transport through the porous membrane structure as individual particles and fouling decreases as the result of the formation of a porous cake [24,25]. On the other hand, the stabilizers themselves can be foulants; they can be retained by the membrane, increasing the thickness of the fouling layer, meanwhile also reducing the porosity of the formed filtration cake by filling the voids between the nanoparticles in the cake [26–28]. Furthermore, polymeric stabilizers may lead to more severe pore clogging due to flocculation bridging, which increases the size of the nanoparticles. Moreover, steric stabilization may not prevent nanoparticles from depositing on the membrane surface either [29]. Therefore, the presence of stabilizers may well result in a higher filtration resistance.

To date, however, there have been no systematic studies of the role of polymeric steric stabilizers during membrane filtration of engineered nanoparticles as far as we know. Therefore, the aim of the research we report here was to determine the effect of steric stabilizers (in this case, polyvinylpyrrolidone (PVP)) on fouling and rejection during microfiltration of nanoparticles. The emphasis of the study was on concentration and chain length (molecular weight) of the PVP and on applied filtration pressure. Whether the stability of the suspension becomes increased or reduced is a function of stabilizer type, concentration and molecular mass (in addition to pH and ionic strength). These properties can therefore strongly affect filtration behavior. The idea behind our work was that combining rejection and permeability data with mixture properties would allow us to identify mechanisms involved in fouling and rejection during microfiltration of sterically stabilized nanoparticle suspensions.

## 2. Theory

### 2.1. Steric stabilization and flocculation

Steric stabilization of nanoparticle suspensions is a matter of finding and maintaining a delicate balance. Adsorption of the stabilizer onto the surface of nanoparticles changes their surface properties. At high enough polymer concentrations, this leads to the nanoparticles being covered with a dense polymer layer. Steric repulsion between polymer chains on the particle surfaces (Fig. 1a) prevents particle aggregation. On the other hand, at low polymer concentrations or with very long polymer chains (high molecular weight), a single polymer can adsorb onto more than one single nanoparticle. This so-called flocculation bridging (Fig. 1b) leads to the formation of clusters of polymer chains and nanoparticles, effectively promoting the aggregation of the nanoparticles [30,31].

In solutions, there is always an equilibrium between the amount of adsorbed stabilizer and the bulk concentration of the stabilizer [32–34]. At increased concentrations of polymer in the bulk, more polymer chains adsorb onto the nanoparticles. As a result, the conformation of the adsorbed polymer chains changes, as schematically shown in Fig. 2. The trains conformation that occurs at lower polymer concentrations changes to a loops and tails conformation at higher polymer concentrations. The adsorbed polymer chains become more elongated and the nanoparticle size increment as a result of stabilizer adsorption is greater.

### 2.2. Dead-end microfiltration of nanoparticles

In previous work [10], we found that constant pressure dead-end microfiltration of electrostatically stabilized suspensions of nanoparticles much smaller than the membrane pores takes place in the following stages: (1) adsorption, (2) free transport of the nanoparticles through pores, (3) pore blockage, (4) cake filtration, and (5) maturation of the cake. Since these filtration stages can only occur in a specific order and permeability decays at a different rate during each of these stages, they can be easily recognized in the filtration curve (Fig. 3a). Pore blockage and formation of the filtration cake, which acts as a secondary membrane, lead to a final nanoparticle rejection to about 90%, as visible in Fig. 3b.

## 3. Materials and methods

### 3.1. Materials

Colloidal silica nanoparticles Ludox TM-50 with a diameter of about 25 nm [10] were used as model nanoparticles. We purchased three types of polyvinylpyrrolidone (PVP), each with a different molecular mass; their average molecular masses were 10 kDa, 40 kDa and 360 kDa (Sigma Aldrich supplier data). Aqueous solutions of ACS grade HCl or NaOH, and NaCl, (Sigma Aldrich) were used to adjust the pH and ionic strength of the solutions, respectively. All solutions were prepared with ultrapure water (Milli-Q, resistivity $> 18.2$ MΩ cm); all chemicals were used without further purification.

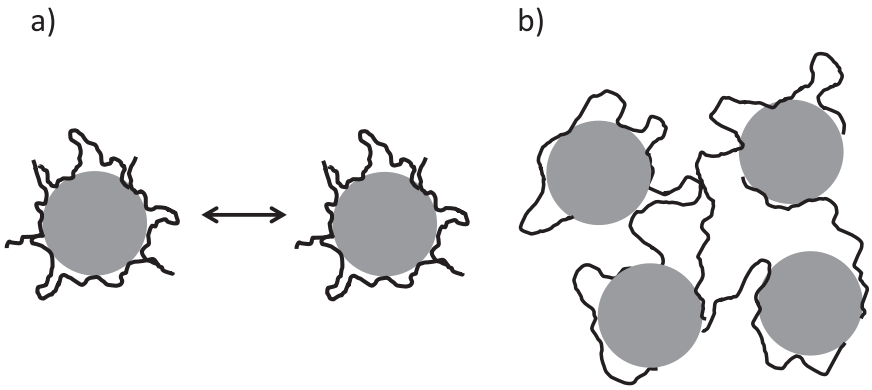


**Fig. 1.** Schematic representation of (a) steric stabilization and (b) flocculation bridging.

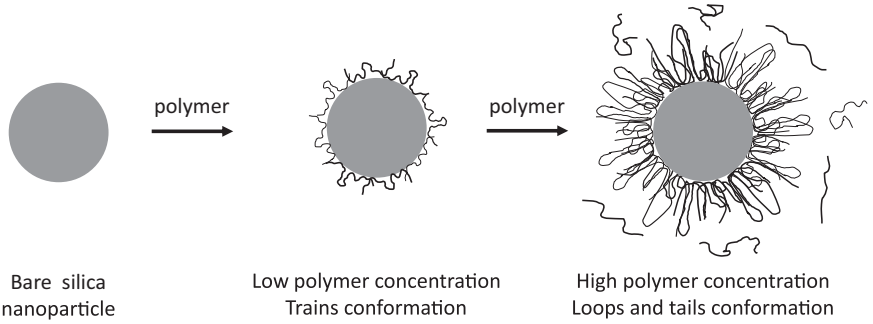


**Fig. 2.** Schematic representation of concentration-dependent conformation change of adsorbed polymer molecules (such as PVP) onto a silica nanoparticle surface (adapted from [34]).

### 3.2. Feed solution characterization

The surface zeta potential of the nanoparticles and their mixtures with PVP were obtained by electrophoretic mobility measurements (Malvern ZetaSizer 3000Hsa). The measurements were carried out with a $50 \pm 1$ mg/L nanoparticle suspension with pH 8, prepared by dilution of the stock silica suspension in Milli-Q water. The hydrodynamic diameter of the nanoparticles in the mixture with PVP was determined in batch mode with a DAWN-Heleos-8 Multi-Angle static Light Scattering (MALS) detector placed at an angle of 108°; a dynamic light scattering (DLS) apparatus (NanoStar, Wyatt Technology Corporation, USA) was connected via a glass fiber cord. We used a fixed angle optical reflectometer equipped with a stagnant point flow cell to obtain information on the adsorption of PVP molecules to the silica surface [35]. For this purpose, we prepared 0.1 g/L PVP suspensions at 1 mM NaCl ionic strength and pH 8 and let them adsorb onto a piranha-treated silicon wafer with a ~75 nm $SiO_2$ top layer. A polarized light beam generated by a He–Ne laser (628 nm) hitting the wafer was reflected around the Brewster angle ($\theta = 71°$) to the detector. The detector measured the intensity of the parallel ($R_p$) and perpendicular ($R_s$) components of the light after the reflection from the surface. The ratio between $R_p$ and $R_s$ gives the measurement signal value $S$(–), which is directly proportional to the adsorbed amount $\Gamma$ (mg/m$^2$) according to Eq. (1):

$$\Gamma = \frac{S - S}{S_0} \cdot Q \tag{1}$$

where $S_0$(–) is the baseline signal, and $Q$ (mg/m$^2$) is an instrument- and material-dependent sensitivity factor. In order to estimate the sensitivity factor $Q$, we used an optical model, which was calculated with the aid of "Professor Huygens" software (Dullware Software). The input parameters for the model were the following: $\theta = 71°$, $n_{SiO_2} = 1.46$, $n_{Si} = 3.85$, $n_{H_2O} = 1.3327$, $d_{SiO_2} = 75$ nm, $dn/dc = 0.175$ mL/g [36]. The calculated sensitivity factor $Q$ was 27 mg/m$^2$ for all experiments. We repeated the reflectometry measurements three times for each molecular mass of PVP.

Asymmetric flow field flow fractionation (AF4) in combination with light scattering (LS) and differential refractive index measurements (dRI) enabled us to extract detailed information about the composition of the feed solutions. The AF4 setup separates colloidal suspensions into fractions, and directly measures the concentration and size of the species in each fraction [37]. Fig. S1 in the Supplementary material shows a schematic diagram of our AF4 setup.

A detailed explanation of the principles behind this method can be found elsewhere [37]. Briefly, the AF4 channel fractionates particles according to their size as described by Eq. (2):

$$t_r \frac{\pi \eta t_v W^2 \phi_X}{kTV_c} \cdot r_h \tag{2}$$

here, $t_r$ is retention time (s), $t_v$ is the retention time of the void peak (s), $w$ is the height of the channel (m), $\phi_x$ is the applied cross-flow (m$^3$/s), $V_c$ is the volume of the channel (m$^3$), $\eta$ is the viscosity (Pa s), $T$ is the temperature (K), $k$ is the Boltzmann constant ($1.38 \cdot 10^{-23}$ J/K), and $r_h$ is the hydrodynamic radius (m). Eq. (2) means that in the ideal case, i.e. in the absence of particle–membrane interactions, the nanoparticle elution time is proportional to nanoparticle size.

After fractionation, the nanoparticles were further characterized with the aid of a light scattering detector and dRI detector, which measured size and concentration of the fractions, respectively. Scattering of light is due to the optical inhomogeneity of suspensions. The intensity of the scattered light is given by the Rayleigh equation:

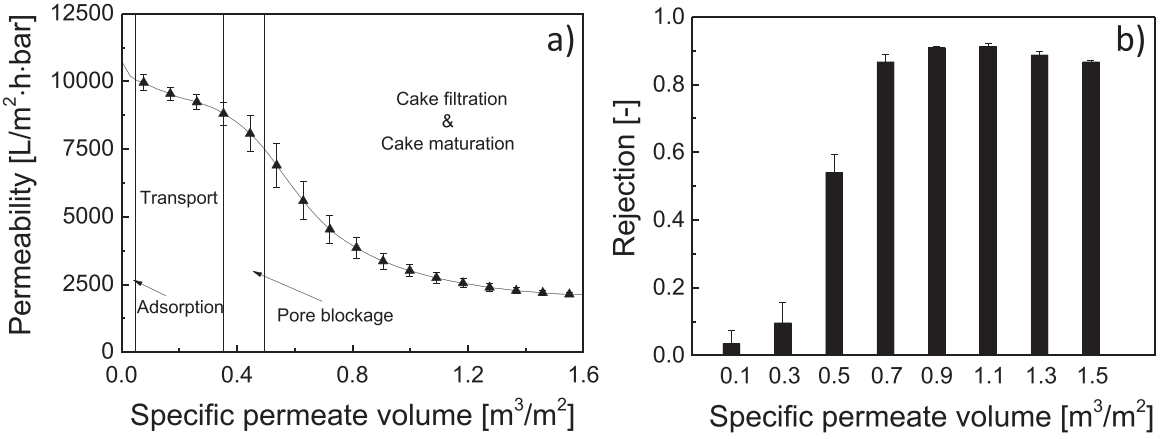


**Fig. 3.** (a) Permeability and (b) rejection of silica nanoparticles as a function of specific permeate volume during microfiltration of 2 mg/L of bare silica nanoparticles [10].

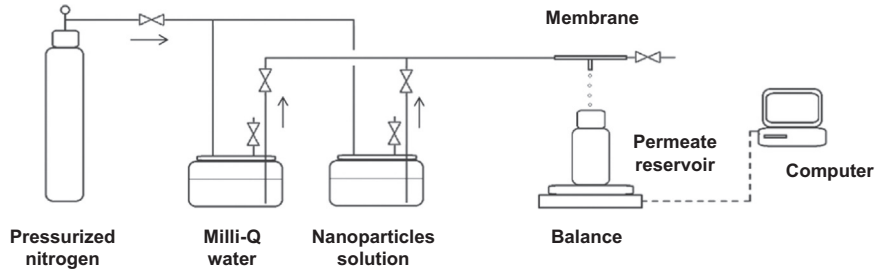


**Fig. 4.** Flow sheet of the used constant pressure filtration setup.

$$i_\theta = I_0\left(n_d^2 - n_m^2\right)\frac{2\pi^2 N v^2}{l^2\lambda_0^4} \tag{3}$$

here $i_\theta$ is the light scattering intensity at angle $\theta$ (W/m$^2$), $I_0$ is the intensity of the incoming light (W/m$^2$), $n_d$ and $n_m$ are the refractive index of particle and medium, respectively, $l$ is the detector distance from the beam (m), $N$ is the number of particles per cubic meter of scattering volume (particles/m$^2$), where each particle has a volume $v$ (m$^3$), and $\lambda$ is the wavelength (nm). The Rayleigh equation predicts that light scattering depends strongly on particle radius $r$ as $v^2 \sim r^6$. We report our light scattering data in terms of the Rayleigh ratio $R_\theta$ (1/cm):

$$R_\theta = \frac{i_\theta}{I_0} l^2 \tag{4}$$

This can be regarded as the relative light scattering per steradian.

For the AF4 experiments, the Eclipse 2 AF4 system (Wyatt Technology Europe GmbH, Germany) was connected to an Agilent 1100 HPLC isocratic pump and a micro-vacuum degasser (Agilent Technologies, Inc.). The fractionation of the nanoparticle mixtures took place in a short fractionation channel (channel length = 152 mm; maximal channel width = 11.5 mm) equipped with a 5 kDa regenerated-cellulose flat sheet membrane (Microdyn-Nadir GmbH, Germany) and a laser-cut spacer with a thickness of 350 µm. The AF4 system was connected in-line with an Optilab rEX variable differential RI (dRI) detector (Wyatt Technology Corporation, USA) and a DAWN Heleos-8 multi-angle light scattering (MALS) instrument (Wyatt Technology Corporation, USA). The DAWN-Heleos-8 instrument was placed at an angle of 108°, where a dynamic light scattering (DLS) apparatus (NanoStar, Wyatt Technology Corporation, USA) was connected via a glass fiber cord. We operated the MALS and dRI detectors at a laser wavelength of 658 nm. All data logging and calculations were performed by Astra 6.1 software (Wyatt Technology Corporation, USA).

Table S1 (Supplementary material) details our AF4 operating procedure for fractionating mixtures of silica nanoparticles and PVP molecules. We used a channel flow of 1 mL/min and an injection flow of 0.2 mL/min. To obtain reasonable retention times and because of the different molecular weights of the PVP, we had to apply different cross-flow rates $V_x$; for 10 kDa and 40 kDa PVP, we used a cross-flow of 0.8 mL/min, whereas a cross-flow of 0.2 mL/min was chosen for 360 kDa PVP.

Because of the AF4 detection limits, the concentrations of silica nanoparticles and PVP were higher in the AF4 experiments than in the filtration experiments, but the concentration ratios were the same.

### 3.3. Membrane and membrane characterization

We used commercially available inside-out PES-PVP microfiltration (MF) hollow-fiber membranes Pentair X-Flow 1.5MF02 (Pentair X-Flow BV, the Netherlands). One membrane fiber was potted in a PVC tube with two component polyurethane glue 2K Expert (Bison International B.V., the Netherlands) to give a final filtration area of 2.5 cm$^2$. The clean-water permeability of the membrane was determined as $11 \cdot 10^3$–$12 \cdot 10^3$ L/m$^2$ h bar. The average pore diameter of the membrane was measured with a Porolux™ 1000 (POROMETER nv) using Porefil Wetting Fluid (supplied by POROMETER nv) as pore-filling liquid. A SurPASS electrokinetic analyzer (Anton Paar GmbH) was used to determine the zeta potential of the inner surface of the membrane, with a 5 mM KCl solution as electrolyte. The zeta potential was calculated according to the Fairbrother–Mastin equation.

### 3.4. Filtration experiments and data processing

All filtration experiments were carried out in a constant pressure filtration setup as depicted in Fig. 4.

A constant pressure of either 0.1 bar, 0.2 bar or 0.4 bar was applied as driving force in the filtration experiments, using pressurized nitrogen. Each filtration experiment consisted of two steps. Firstly, 50 mL of Milli-Q water was filtered through the membrane module to obtain a stable clean-water flux. Secondly, after filtration of 50 mL of Milli-Q water, we connected the nanoparticles solution vessel to the membrane module by opening the valve. During each filtration experiment, 400 mL of a feed solution was filtered. The cumulative mass increment of the permeate was monitored continuously by an analytical balance connected to the computer. The permeability was calculated according to Eq. (5):

$$L_P = \frac{J}{\Delta P} \tag{5}$$

where $L_P$ is the liquid permeability (L/m$^2$ h bar), $J$ is the flux (L/m$^2$ h) and $\Delta P$ is the transmembrane pressure (bar). Permeate samples were collected every 50 mL for ICP-MS analysis (Thermo Fisher Xseries 2). We calculated rejection of the silica nanoparticles according to Eq. (6):

$$\sigma = 1 - \frac{C_p}{C_f} \tag{6}$$

where $\sigma$ is the rejection (–), $C_P$ is the concentration of the nanoparticles in the permeate sample (mg/L), and $C_f$ is the concentration of the nanoparticles in the feed solution (mg/L).

We prepared Milli-Q water solutions with pH 8 and containing 1 mM NaCl, 2 mg/L of silica nanoparticles and different concentrations of PVP. Three types of PVP, each with a different molecular mass (10 kDa, 40 kDa and 360 kDa), were used in this study to evaluate the effect of PVP chain length on filtration and fouling during filtration of silica nanoparticle suspensions. To determine the role of the PVP concentration in the fouling behavior, we also used different concentrations of PVP in the feed solution for each molecular mass of the polymer (1 mg/L, 2 mg/L and 4 mg/L). The effect of transmembrane pressure on filtration performance was evaluated by application of lower (0.1 bar) and higher (0.4 bar)

transmembrane pressures, in addition to the standard 0.2 bar. The applied transmembrane pressure resulted in clean water fluxes of approx. 1150 L/m$^2$ h, 2300 L/m$^2$ h and 4600 L/m$^2$ h for 0.1 bar, 0.2 bar and 0.4 bar, respectively. These initially high clean water fluxes decrease with filtration time and deposition of the nanoparticles on the membrane surface. By applying the same initial conditions in all filtration experiments we can elucidate the role of the polymeric stabilizer in fouling development of nanoparticles.

## 4. Results and discussion

The results and discussion section consists of two subsections. In the first subsection, we describe the detailed characterization of the membrane and the feed solutions. With regard to the feed solutions, it is especially important to understand how the presence of the stabilizing polymer influences the stability of the nanoparticle suspension. In the second subsection, we discuss the filtration experiments performed with the described feed solutions. The observations described in the first subsection enable the interpretation of the results reported in the second subsection.

### 4.1. Characterization of membrane and feed solutions

#### 4.1.1. Membrane

Table 1 lists the experimentally obtained properties of the MF membrane. The average pore diameter of this membrane as measured with capillary flow porometry (CFP) is $200 \pm 15$ nm. Streaming potential measurements showed that the inner surface of the membrane was negatively charged at pH 8 and had a zeta potential of $-23.1 \pm 2.1$ mV.

#### 4.1.2. Stabilizers and nanoparticles

Table 2 lists the characteristics of the nanoparticles and PVP stabilizers. Similar to the membrane surface, the surface of the nanoparticles also is negatively charged at pH 8 ($-36 \pm 1.2$ mV) because of the silanol groups of these silica particles [38].

PVP molecules are able to adsorb onto a silica surface via the formation of hydrogen bonds between the silanol groups and the PVP monomers [36,40]. The reflectometer data in Table 2 confirm the adsorption of PVP onto the silica surface for the pH and ionic strength used in this investigation. Fig. 5a shows the zeta potential of the nanoparticles as a function of the PVP concentration. For all three used molecular masses of PVP, the zeta potential becomes less negative with increasing PVP concentration. As a layer of polymer forms on the nanoparticles, the shear plane at which the zeta potential is measured moves away from the particle interface. Although the actual surface charge of the particle remains unchanged, adsorption of the PVP molecules screens strong negative surface charge of the silanol groups on the nanoparticle surface. Furthermore, the greater distance to the shear plane means a less negative zeta potential. The higher the molecular mass of the PVP, the smaller the zeta potential, indicating the presence of a thicker polymer layer on the nanoparticle surface [41]. Fig. 5b shows a similar trend for the change in hydrodynamic diameter of the nanoparticles with PVP concentration. The diameter increases with increasing PVP concentration, and this is more pronounced for higher molecular masses of PVP.

#### 4.1.3. Asymmetric flow field flow fractionation of the feed solutions

The properties of the stabilizer adsorbed onto the silica nanoparticles determine the stability of the particles in the suspension, and hence the particles' filtration behavior. As Fig. 5 illustrates, molecular mass and concentration of the PVP stabilizer change the nanoparticles' properties, and as a result can alter fouling development. However, measurements of zeta potential and hydrodynamic diameter in the bulk do not give complete information about the number of solute fractions present in the solution, their sizes and their concentrations. In view of the importance of nanoparticle size, size distribution and stability and to be able to correlate the filtration behavior of silica nanoparticles with the role of the PVP stabilizer, obtaining detailed information about concentration and size of the solute fractions is essential. For that reason, we fractionated the silica–PVP mixtures by using the AF4 technique, followed by a detailed characterization of the obtained fractions.

Fig. 6 displays chromatograms for the fractionated solutions containing 50 mg/L of silica nanoparticles and PVP. Fig. 6a and b

**Table 1**
Properties of the used membrane.

| **Membrane** | | | | |
|---|---|---|---|---|
| Type | Material | Clean water permeability [L/m$^2$ h bar] | Pore size [nm] | Zeta potential at pH 8 [mV] |
| Pentair X-Flow 1.5MF02 | PES/PVP | $11 \pm 1 \cdot 10^3$ | $200 \pm 15$ | $-23.1 \pm 2.1$ |

**Table 2**
Properties of the used silica nanoparticles and PVP stabilizers.

| **Nanoparticles** | | | |
|---|---|---|---|
| Type | Diameter [nm] | Surface area [m$^2$/L][a] | Zeta potential at pH 8 [mV][b] |
| Ludox TM 50 | $25 \pm 5.2$ [10] | 0.28 | $-36 \pm 1.2$ |
| **Stabilizers** | | | |
| Type | $M_w$ [kDa][a] | Hydrodynamic diameter [nm] | Adsorption to silica[b] [mg/m$^2$] |
| PVP10 | 10 | 4.3 [39] | $0.64 \pm 0.1$ |
| PVP40 | 40 | 10.2 [39] | $0.62 \pm 0.09$ |
| PVP360 | 360 | 39.9 [39] | $0.67 \pm 0.1$ |

[a] Manufacturer's data.
[b] Experimental data.

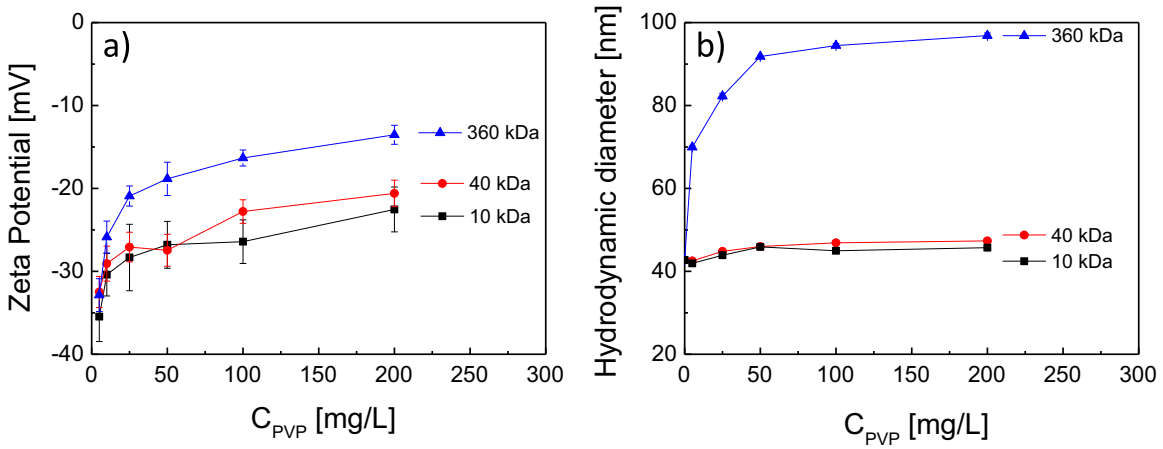


**Fig. 5.** (a) Zeta potential and (b) hydrodynamic diameter of silica nanoparticles as a function of PVP concentration and PVP molecular mass.

gives results for mixtures with 10 kDa PVP; Fig. 6c and d shows results for mixtures with 40 kDa PVP. For the solutions containing 360 kDa PVP (Fig. 6e and f), we reduced the applied cross-flow velocity to 0.2 mL/min (see Table S1) to obtain reasonable elution times. For this reason, we cannot compare these chromatograms directly with those for 10 kDa and 40 kDa PVP solutions, so we discuss the results for 360 kDa PVP separately.

The Rayleigh ratio, which is plotted in Fig. 6a, increased after the addition of 10 kDa PVP to the nanoparticle suspension, suggesting an increase of the nanoparticles' diameter. However, the shape of the chromatogram peaks for bare nanoparticles is the same as for nanoparticles coated with 10 kDa PVP molecules, which implies that both solutions had a comparable size distribution. Furthermore, as Fig. 6a shows, increasing the 10 kDa PVP concentration only led to a slight increase of the elution time (linearly related to nanoparticle size; see Eq. (2)). This suggests that the nanoparticle size barely increased and that nanoparticle aggregation remained very limited when 10 kDa PVP was added. These findings are supported by Fig. 5b, which shows that adsorption of 10 kDa PVP led only to a slight increase of the hydrodynamic diameter.

On the other hand, Fig. 6c clearly demonstrates that the elution time for silica nanoparticles increased with increasing amount of added 40 kDa PVP. Adsorption of 40 kDa PVP molecules resulted in a marked increase of the radius of the nanoparticles, and this increase was larger with increasing polymer concentration. When comparing Fig. 6a and c, we can see that the hydrodynamic radius of the nanoparticles (as deduced from the nanoparticle elution time) increased more with increasing concentration when longer polymer chains were added. The static light scattering results obtained for 10 kDa PVP and 40 kDa PVP (Fig. 6a and c), dRI chromatograms (Fig. 6b and d) and dynamic light scattering results (Fig. 5b) suggest the conformational change of adsorbed PVP chains as described in Section 2.1 and Fig. 2. As a result, slightly longer elution times were needed for a higher concentration and higher molecular mass of the polymer.

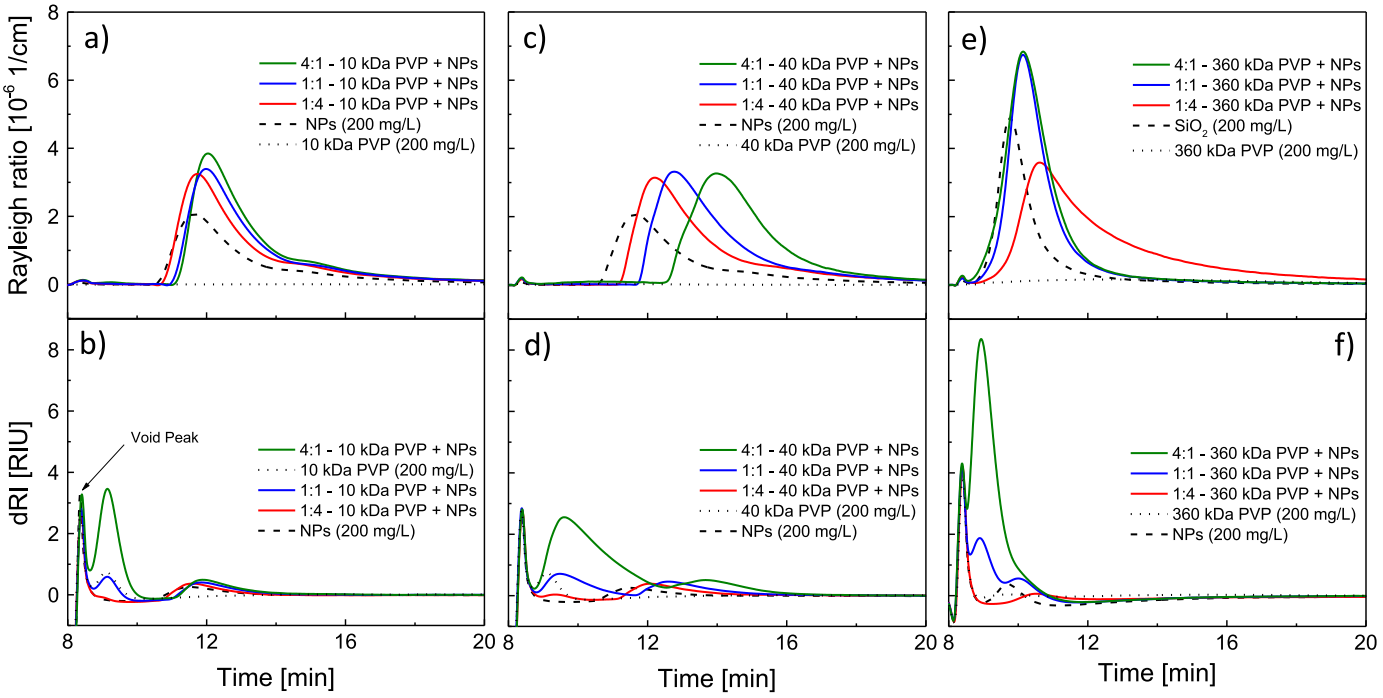


**Fig. 6.** Rayleigh ratio and differential refractive index (dRI) obtained for asymmetric flow field flow fractionation of silica nanoparticle–PVP mixtures. (a) Rayleigh ratio and (b) differential refractive index for 10 kDa PVP; (c) Rayleigh ratio and (d) differential refractive index for 40 kDa PVP; (e) Rayleigh ratio and (f) differential refractive index for 360 kDa PVP.

In Fig. 6b and d, the differential refractive index is plotted as a function of elution time for mixtures of silica nanoparticles and 10 kDa and 40 kDa PVP, respectively. For each PVP–silica nanoparticle mixture, not one but two distinct peaks are visible. This is in contrast with the light scattering chromatograms (Fig. 6a and c), which show only one peak. The second, less intensive peaks in the two dRI chromatograms overlay the light-scattering peaks (Fig. 6a and c), which can be attributed to the silica nanoparticles. Similarly to LS peaks (Fig. 6a and c), elution time of this second peak increases with increasing PVP concentration (Fig. 6b and d). The first dRI peaks in Fig. 6b and d, which increase significantly with increasing concentration of PVP, represent unadsorbed PVP molecules since these peaks eluted at the same time as pure PVP. Furthermore, the area of these peak scales up linearly with increasing PVP concentration in the suspension. The presence of the two distinct peaks for mixtures of 10 kDa or 40 kDa PVP and silica nanoparticles proves the coexistence of two fractions: silica nanoparticles coated by PVP molecules and free, unadsorbed PVP molecules.

In the case of 360 kDa PVP, a clear distinction between the nanoparticle and PVP peaks is only possible for the 1:1 concentration ratio. For the lowest concentration of 360 kDa PVP (50 mg/L, 1:4 ratio), the nanoparticle peak shifts to a longer elution time (Fig. 6e and f), suggesting the presence of larger nanoparticles. For a greater 360 kDa PVP concentration (200 mg/L, 1:1 ratio), two distinct peaks can be observed: first the polymer peak and then the nanoparticle peak. Furthermore, the mixture of nanoparticles and PVP molecules starts to elute faster with increasing concentration (Fig. 6e), the intensity of the peaks is higher, and the peaks are less broad than for the lowest concentration of PVP. We attribute this to a slight restabilization of the silica nanoparticles at the higher 360 kDa PVP concentrations. At lower 360 kDa PVP concentrations, the long polymer chains caused reversible flocculation bridging between the nanoparticles, which resulted in longer elution times. With further increased concentrations of 360 kDa PVP, more polymer was adsorbed to the nanoparticles and they became restabilized. In addition, as observed for 10 kDa and 40 kDa PVP, increased concentrations of 360 kDa PVP led to the first dRI peak becoming larger, indicating a higher concentration of free polymers (Fig. 6f). To summarize, the AF4 results clearly show that our PVP–silica nanoparticle mixtures consisted of two fractions, namely PVP-coated nanoparticles and free unadsorbed polymer chains. With increased PVP concentrations, more polymer adsorbed on the surface of the nanoparticles, resulting in an increase in nanoparticle size (hydrodynamic diameter). This increase was greater for higher molecular masses of the PVP. Furthermore, higher PVP concentrations led to a higher concentration of unadsorbed polymer chains. No aggregation of nanoparticles was observed for all used concentrations of 10 kDa PVP and 40 kDa PVP. In the case of 360 kDa PVP, flocculation bridging appeared to occur when the concentration was 50 mg/L of PVP (1:4 ratio). In view of the limited aggregation and only slight increase of the nanoparticle diameter in the mixtures with 10 kDa PVP and 40 kDa PVP, we do not expect increased pore blockage and nanoparticle rejection to occur during filtration of those mixtures. On the other hand, at higher PVP concentrations, the presence of free PVP polymer chains might contribute to pore blockage and densification of the cake layer. For 360 kDa PVP, pore blockage might occur faster due to flocculation bridging and the higher molecular mass of the polymer.

### 4.2. Filtration experiments

#### 4.2.1. Filtration of nanoparticles and low-molecular-weight PVP stabilizer

We first investigated the influence of the concentration of 10 kDa PVP stabilizer on dead-end microfiltration of the silica nanoparticles. Fig. 7 summarizes the filtration results. Fig. 7a shows that for bare nanoparticles without added PVP (the lowest line), the permeability decreased significantly during the course of filtration. Fouling developed in the five stages as described in Section 2. The general shape of the filtration curves obtained with addition of 10 kDa PVP is comparable to this for bare silica nanoparticles. After adding 4 mg/L 10 kDa PVP without nanoparticles, the permeability decreased by about 20% compared with the initial permeability and distinct fouling stages could no longer be observed. This difference in fouling behavior of silica nanoparticles and 10 kDa PVP is related to their size difference (see Table 2).

However, as also visible in Fig. 7a, even the addition of a small amount of 10 kDa PVP (1 mg/L) to the nanoparticle solution already extended the duration of nanoparticle transport through the membrane pores (stage 2), and pore blockage was initiated later. As Table 3 presents, the estimated blocking point (point at which pore blocking starts) [10] for 1 mg/L of 10 kDa PVP occurred after about $0.31 \pm 0.01$ m$^3$/m$^2$. For bare nanoparticles, this was $0.23 \pm 0.03$ m$^3$/m$^2$. The duration of the nanoparticle transport stage was even longer for 2 mg/L of 10 kDa PVP ($0.35 \pm 0.02$ m$^3$/m$^2$). However, it shortened when the concentration of 10 kDa PVP stabilizer increased to 4 mg/L; pore blocking then started after about $0.23 \pm 0.02$ m$^3$/m$^2$.

The longer transport stage observed with a higher specific permeate volume at the blocking point $V_{block}$ for 1 mg/L and 2 mg/L 10 kDa PVP coated nanoparticles can be explained by enhanced nanoparticle stabilization caused by adsorption of the short PVP

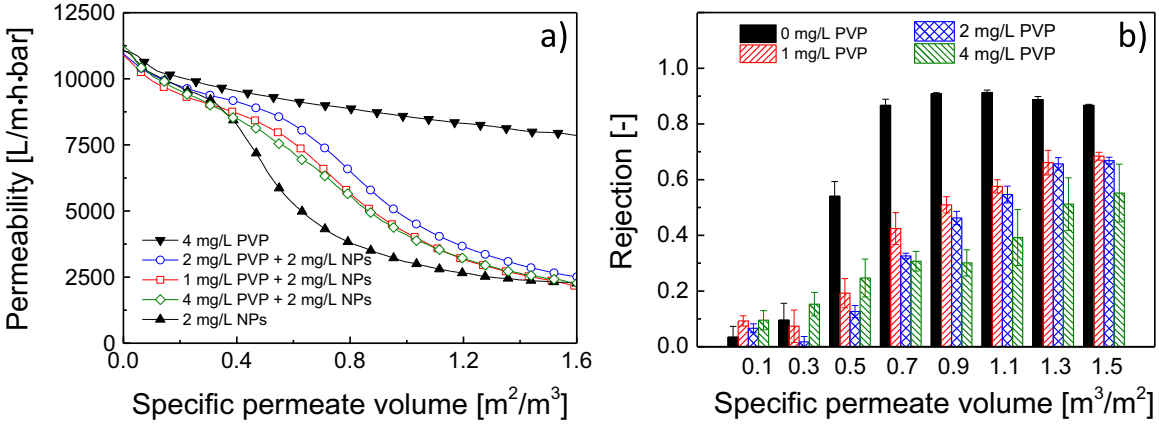


**Fig. 7.** (a) Permeability and (b) nanoparticle rejection as a function of specific permeate volume during filtration of 2 mg/L of silica nanoparticles with various concentrations of 10 kDa PVP at a transmembrane pressure of 0.2 bar.

**Table 3**
Blocking points ($V_{block}$) describing transition between transport stage and pore blockage stages for bare and PVP coated nanoparticles.

| PVP concentration [mg/L] | | 0 | 1 | 2 | 4 |
|---|---|---|---|---|---|
| $V_{block}$ [$m^3/m^2$] | 10 kDa | $0.23 \pm 0.03$ | $0.31 \pm 0.01$ | $0.35 \pm 0.02$ | $0.23 \pm 0.02$ |
| | 40 kDa | $0.23 \pm 0.03$ | $0.21 \pm 0.01$ | $0.31 \pm 0.02$ | $0.25 \pm 0.04$ |
| | 360 kDa | $0.23 \pm 0.03$ | na | na | na |

na = not available due to instantaneous pore blocking.

chains. High stability of the nanoparticles reduces their near-membrane-surface aggregation induced by the convective drag force, so maintaining a dispersed state of nanoparticles and consequently it takes longer before pore blocking sets in. The stabilization effect of the polymer molecules increases with PVP concentration since coverage of the nanoparticle surface is higher [41]. During filtration, however, the free PVP molecules can also cause membrane fouling. In the case of 4 mg/L of 10 kDa PVP, the free PVP chains (detected by AF4; see Fig. 6b) clearly contributed to pore blockage; hence, the duration of the nanoparticle transport decreased to $0.23 \pm 0.05$ $m^3/m^2$.

During the pore blockage stage, rejection of the bare nanoparticles rose sharply from about 10% to about 90% for pure nanoparticles (see Fig. 7b, black columns). However, when 10 kDa PVP was present in the feed solution, rejection of the nanoparticles became significantly reduced and developed continuously to about 70% at the end of the filtration. The increased nanoparticle transport through the membrane pores and delayed pore blockage (see Table 3) with10 kDa PVP addition led to lower nanoparticle rejection. This caused less accumulation of nanoparticles on the membrane; hence, assuming equal cake layer porosity, the cake layer was thinner. In addition, the presence of free 10 kDa PVP chains (see Fig. 6b) may have changed the packing order of the cake. McDonogh et al. [42] demonstrated that polydispersed suspensions of charged nanoparticles can form filtration cakes in which nanoparticle packing is not uniform. The voids, defects and channels in the filtration cake structure allow transport of nanoparticles through the cake, resulting in less nanoparticle rejection. In our case as well, the feed solution consisted of solutes, which differed in size (free polymer 10 kDa PVP chains and nanoparticles coated with 10 kDa PVP). The surface charges responsible for nanoparticle repulsion were replaced by steric repulsions introduced by 10 kDa PVP chains. In the same time, these polymer chains work against ordered packing of the cake. Furthermore, increasing the concentration of 10 kDa PVP caused less rejection of nanoparticles, as is visible in Fig. 7b, so the 10 kDa PVP chains clearly caused lower rejection.

*4.2.2. Filtration of nanoparticles with added higher-molecular-weight PVP stabilizer*

Fig. 8a and b displays permeability and rejection data for filtration of silica nanoparticles with 40 kDa PVP as stabilizer, respectively. As in the experiments with 10 kDa PVP, the addition of 40 kDa PVP stabilizer influenced permeability decay and rejection of silica nanoparticles, but there are only minor differences with the 10 kDa case.

The initial stabilization (time until $V_{block}$) of the filtration curve in Fig. 8a, signifying transport of the nanoparticles through the membrane pores, only lasted longer when 2 mg/L 40 kDa PVP was added (see Table 3). No effect on the permeability in this initial filtration stage was observed for 1 mg/L and for 4 mg/L of 40 kDa PVP. A synergic fouling effect of the nanoparticles and 40 kDa PVP molecules might explain this behavior. Firstly, the bulkier unadsorbed 40 kDa PVP molecules (diameter of about 10 nm; Table 2) may have contributed strongly to blockage of membrane pores. Secondly, adsorption of the longer 40 kDa PVP chains to silica nanoparticles caused a larger increase of the nanoparticle size than for 10 kDa PVP, as shown in Fig. 6c and a, so the difference between the nanoparticle diameter and the pore diameter became smaller. As a consequence, the pore blockage stage occurred sooner, despite the improved steric stabilization of the nanoparticles.

Similarly, as for 10 kDa PVP, rejection of silica nanoparticles became lower after addition of 40 kDa PVP to the feed solution (Fig. 8b). However, overall nanoparticle rejection was greater than with 10 kDa PVP (Fig. 7b). The 40 kDa PVP has longer polymer chains than 10 kDa PVP, and consequently may adsorb onto more than one nanoparticle in the filtration cake (bridging) [43]. This could lead to a more interconnected, more compact structure of the nanoparticle–PVP cake, across which silica nanoparticles cannot be transported that easily. Furthermore, with 40 kDa PVP, the pore blockage and cake filtration stages occurred earlier (see Fig. 8a) than with 10 kDa PVP (see Fig. 7a). Hence, more nanoparticles accumulated on the membrane surface over time, leading to a thicker deposit, in turn resulting in more rejection. This explanation is supported by the fact that delayed pore blockage in

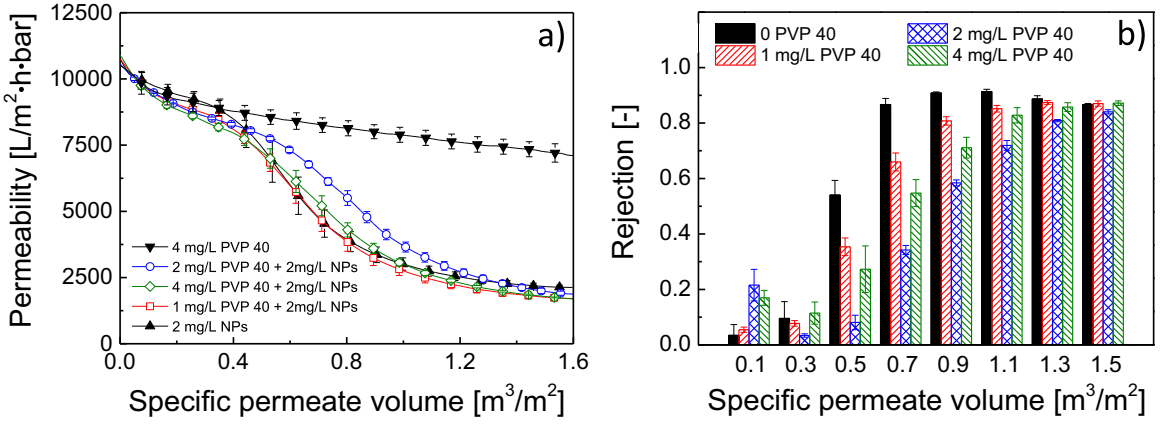


**Fig. 8.** (a) Permeability and (b) rejection of silica nanoparticles as a function of specific permeate volume during filtration of 2 mg/L of silica nanoparticles with various concentrations of 40 kDa PVP at a transmembrane pressure of 0.2 bar.

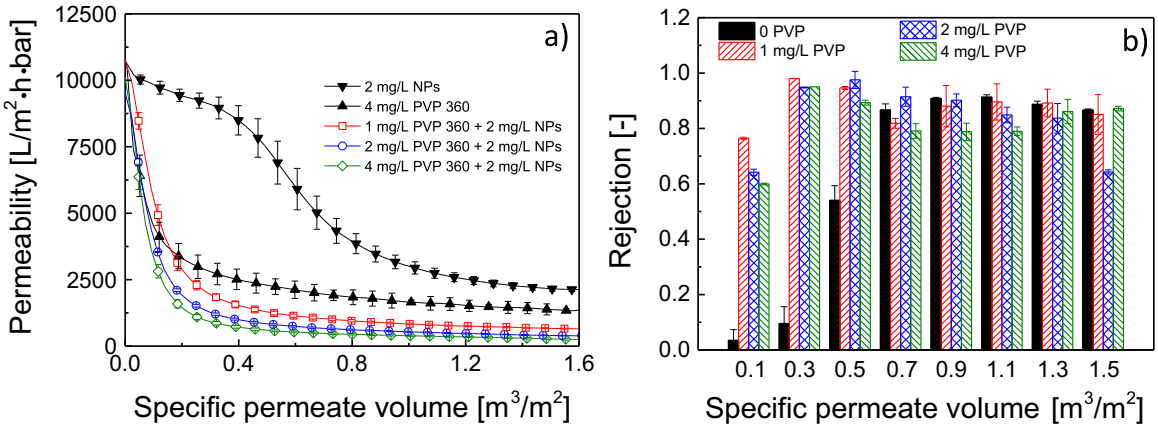


**Fig. 9.** (a) Permeability and (b) rejection of silica nanoparticles as a function of specific permeate volume during filtration of 2 mg/L of silica nanoparticles with various concentrations of 360 kDa PVP at a transmembrane pressure of 0.2 bar.

the case of 2 mg/L of 40 kDa PVP (Fig. 8a) results in a lower rejection of silica nanoparticles during the whole filtration process than with 1 mg/L and 4 mg/L 40 kDa PVP (Fig. 8b), pointing at a synergic effect.

Fig. 9a shows the permeability decay during filtration of silica nanoparticles with varying concentrations of 360 kDa PVP stabilizer. The 360 kDa PVP had an average hydrodynamic diameter almost twice as large (39.9 nm) as that of the silica nanoparticles (25 nm). As Fig. 9a shows, this larger hydrodynamic diameter of PVP caused such a rapid permeability decay due to pore blockage, even for pure polymer, that estimation of the blocking point ($V_{block}$) was impossible. After this immediate pore blockage, cake filtration took place. With the mixtures of 360 kDa PVP and silica nanoparticles, fouling developed even faster and was more severe than with pure polymer or bare nanoparticles. Higher polymer concentrations caused faster pore blockage and a stronger reduction of the permeability during cake filtration because these higher concentrations of 360 PVP significantly increased nanoparticle size (see Fig. 5b). Additionally, the less negative zeta potential (Fig. 5a) and the higher polymer load did likely result in a thicker and more compact nanoparticle deposit [44].

Fig. 9b makes clear that nanoparticle rejection during filtration with 360 kDa PVP was very high (60–80%), even for the first permeate sample. However, there was a slight reduction of this rejection later. This is surprising since we would expect a very high rejection of nanoparticles after the instantaneous pore blockage, and a very low permeability in the later filtration stage. One possible explanation for the decrease in rejection might be extensive concentration polarization occurring inside the fiber from the beginning of the filtration.

#### 4.2.3. Role of transmembrane pressure

The applied transmembrane pressure can play an important role in the filtration of the silica nanoparticles–PVP mixtures, leading to a more compact or a more porous nanoparticle deposit. Therefore, the role of the polymeric stabilizers in the formation of nanoparticle deposits and rejection of nanoparticles may be different at different transmembrane pressures.

Fig. 10 shows permeability and rejection of bare silica nanoparticles for different transmembrane pressures. With a higher transmembrane pressure (0.4 bar) than the reference pressure of 0.2 bar, the flux declined faster in the first fouling stage (Fig. 10a), which can be explained by accelerated nanoparticle aggregation due to a higher convective drag force. Furthermore, this higher drag force compresses the filtration cake, thereby reducing cake porosity, leading to a significantly lower flux at the end of the filtration process. On the other hand, use of a lower transmembrane pressure (0.1 bar) did not significantly affect the duration of the initial nanoparticle transport and pore blockage stages. It enabled maintaining a constant and much higher flux in the cake filtration stage, due to less compression of the cake and thus a more open cake structure.

Unexpectedly, differences in the applied transmembrane pressure and the resulting fluxes did not influence rejection of the nanoparticles after formation of the filtration cake, as shown in Fig. 10b. The rejection of nanoparticles for all applied pressures

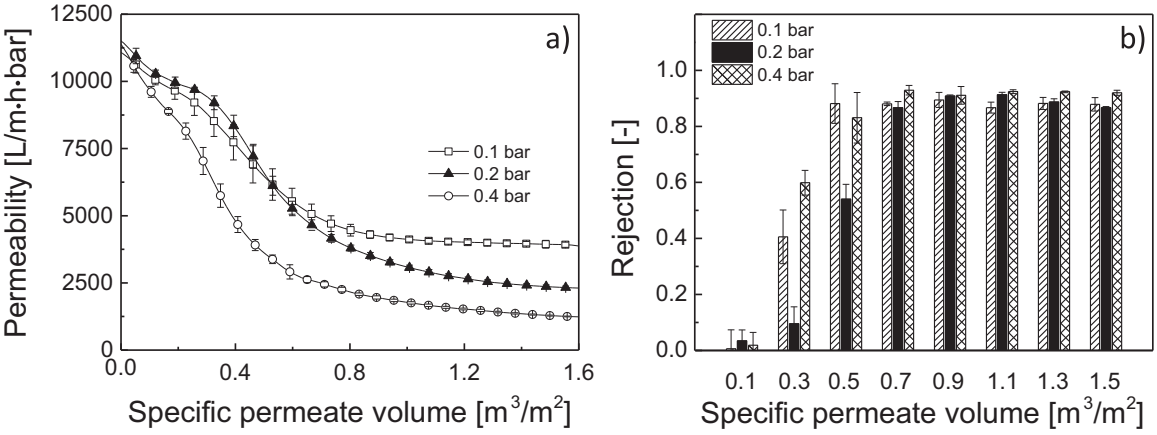


**Fig. 10.** (a) Permeability and (b) rejection of bare silica nanoparticles as a function of specific permeate volume during filtration of 2 mg/L bare silica nanoparticles (no PVP) at various transmembrane pressures.

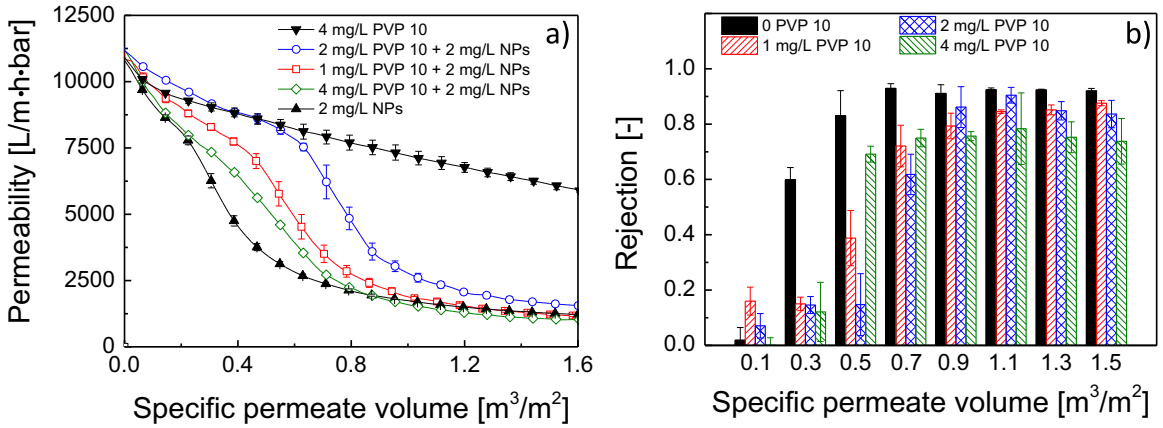


**Fig. 11.** (a) Permeability and (b) rejection of silica nanoparticles as a function of specific permeate volume during filtration of 2 mg/L of silica with various concentration of 10 kDa PVP at a transmembrane pressure of 0.4 bar.

was about 90% from the fourth permeate sample onward (0.7 $m^3/m^2$ specific permeate volume). Apparently, the highly ordered structure of the filtration cake, due to the high monodispersity of the nanoparticles and the strong repulsion among them, did not allow nanoparticle transport, even for very open cake structures (e.g. at 0.1 bar, in our experiments) [42].

When we carried out the filtration at a pressure of 0.4 bar (see Fig. 11a), the addition of 1 mg/L or 2 mg/L 10 kDa PVP had the same stabilization effect as with a pressure of 0.2 bar (see Section 4.2.2), allowing longer transport of nanoparticles through the membrane pores. Addition of 4 mg/L of 10 kDa PVP caused faster pore blockage, and rejection of the nanoparticles was reduced with increasing 10 kDa PVP concentrations (see Fig. 11b), as was the case with 0.2 bar. However, at the end of the filtration test, rejection of the nanoparticles reached values of about 80–90%, which is higher than obtained with 0.2 bar (see Fig. 7b). This higher rejection can be explained by the before-mentioned cake compaction effect of higher transmembrane pressures.

At a transmembrane pressure of 0.1 bar, adding 10 kDa PVP to the silica nanoparticles had a clear impact on fouling development (Fig. 12a). The initial stabilization of the permeability (related to the nanoparticle transport through pores) was less pronounced or did not occur at all. We conclude that the pore blockage stage occurred immediately, since there was no transport stage. This is the result of the lower filtration-driving force at this pressure, which means that the contact time between the nanoparticles and PVP molecules in the concentration polarization zone on the membrane surface was longer. As a result, there was more time for adsorption of PVP molecules onto the nanoparticles at lower 10 kDa PVP concentrations (as visible in Figs. 5a and 6). In the nanoparticle deposit, this may have led to interconnection of nanoparticles by PVP chains [32,33] via flocculation bridging (see Fig. 1b). This effect was less pronounced with higher 10 kDa PVP concentrations due to the higher coverage of the silica surface by polymer. Steric repulsion prevented flocculation bridging and no aggregation was observed, as can be deduced from Fig. 6a. Hence, for increasing 10 kDa PVP concentrations, we observed less permeability decay during the course of filtration (Fig. 12a). On the other hand, the lower zeta potential (Fig. 5a) and the increasing polymer concentration both led to a denser filtration cake. We therefore saw a significantly lower permeability at the end of the filtration with feed solutions containing PVP than with solutions containing bare nanoparticles. However, the nanoparticle deposit obtained with a transmembrane pressure of 0.1 bar was still more permeable for nanoparticles than the deposits obtained with 0.2 bar and 0.4 bar. The lower compaction of the cake and the lower packing order with increasing 10 kDa PVP concentration resulted in lower nanoparticle rejection (Fig. 12b).

## 5. Conclusions

This experimental study investigated fouling and rejection during dead-end microfiltration of silica nanoparticles sterically stabilized with PVP polymers. Adsorption of PVP onto the nanoparticle surface changes nanoparticle interaction from electrostatic

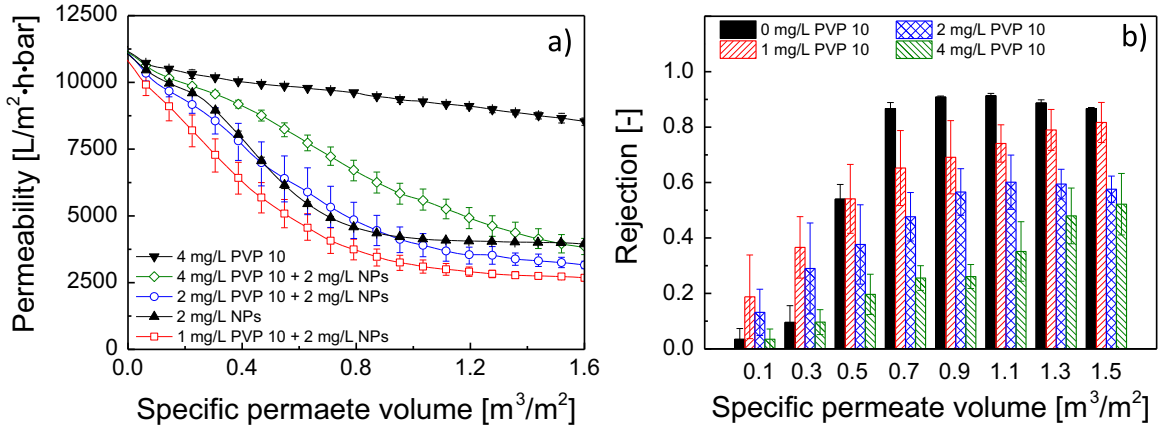


**Fig. 12.** (a) Permeability and (b) rejection of silica nanoparticles as a function of specific permeate volume during filtration of 2 mg/L of silica nanoparticles with various concentrations of 10 kDa PVP and a transmembrane pressure of 0.1 bar.

to steric. Characterization of our feed solutions by AF4 revealed the presence of two fractions, namely free PVP chains and sterically stabilized PVP-coated nanoparticles. Our research confirmed that fouling and rejection behavior of sterically stabilized nanoparticles is strongly determined by the properties of the used stabilizer (in our case, PVP), such as molecular mass and stabilizer concentration. Increasing the concentration of PVP stabilizer with a low molecular weight (10 kDa and 40 kDa) generally appears to result in a higher stability of the nanoparticles, and hence easier transportation of the nanoparticles through membrane pores, without aggregation. However, adding too much PVP stabilizer can result in a synergic fouling effect, where the effect of stabilization of nanoparticles is countered by the higher fouling contribution of the PVP stabilizer itself. Furthermore, nanoparticle rejection drops with increasing PVP stabilizer concentration, suggesting the formation of a more open and permeable cake structure. A higher molecular weight of the stabilizer results in a larger nanoparticle size and can also allow flocculation bridging. Consequently, pore blockage occurs faster and rejection of nanoparticles is greater. Moreover, the contribution of the PVP chains to fouling development increases with increasing molecular mass of the stabilizer. Finally, the transmembrane pressure also exerts control over the structure of the cake layer. Applying a higher transmembrane pressure results in a more compact cake structure, which is less permeable for nanoparticles. Decreasing the transmembrane pressure results in a less dense cake layer; this lowers nanoparticle rejection.

## Acknowledgments

This work was supported by NanoNextNL, a micro- and nanotechnology consortium of the government of the Netherlands and 130 partners. We especially acknowledge Vitens N.V. for the ICP-MS measurements.

## Appendix A. Supplementary material

Supplementary data associated with this article can be found in the online version at http://dx.doi.org/10.1016/j.memsci.2016.01.032.

## References

[1] S.F. Hansen, E.S. Michelson, A. Kamper, P. Borling, F. Stuer-Lauridsen, A. Baun, Categorization framework to aid exposure assessment of nanomaterials in consumer products, Ecotoxicology 17 (2008) 438–447.
[2] H. Weinberg, A. Galyean, M. Leopold, Evaluating engineered nanoparticles in natural waters, Trends Anal. Chem. 30 (2011) 72–83.
[3] P. Westerhoff, G. Song, K. Hristovski, M.A. Kiser, Occurrence and removal of titanium at full scale wastewater treatment plants: implications for $TiO_2$ nanomaterials, J. Environ. Monitor. 13 (2011) 1195–1203.
[4] T.E. Abbott Chalew, G.S. Ajmani, H. Huang, K.J. Schwab, Evaluating nanoparticle breakthrough during drinking water treatment, Environ. Health. Perspect. 121 (2013) 1161–1166.
[5] C.F. Jones, D.W. Grainger, In vitro assessments of nanomaterial toxicity, Adv. Drug Deliv. Rev. 61 (2009) 438–456.
[6] N. Singh, B. Manshian, G.J. Jenkins, S.M. Griffiths, P.M. Williams, T.G. Maffeis, et al., NanoGenotoxicology: the DNA damaging potential of engineered nanomaterials, Biomaterials 30 (2009) 3891–3914.
[7] C. Buzea, I. Pacheco, K. Robbie, Nanomaterials and nanoparticles: sources and toxicity, Biointerphases 2 (2007) MR17–MR71.
[8] K.M. Persson, G. Trägardt, G. Dejmek, Fouling behaviour of silica on four different microfiltration membranes, J. Membr. Sci. 76 (1993) 151–172.
[9] S. Surawanvijit, H.H. Liu, M. Kim, Y. Cohen, Removal of metal oxide nanoparticles from aqueous suspensions, Sep. Sci. Technol. 49 (2014) 161–170.
[10] K. Trzaskus, A.J.B. Kemperman, K. Nijmeijer, Towards controlled fouling and rejection in dead-end microfiltration of nanoparticles – role of electrostatic interactions, J. Membr. Sci. 496 (2015) 174–184.
[11] M. Palencia, B.L. Rivas, H. Valle, Size separation of silver nanoparticles by dead-end ultrafiltration: description of fouling mechanism by pore blocking model, J. Membr. Sci. 455 (2014) 7–14.
[12] S.F. Sweeney, G.H. Woehrle, E. Hutchison, Rapid purification and size separation of gold nanoparticles via diafiltration, J. Am. Chem. Soc. 128 (2006) 3190–3197.
[13] A. Grenier, M. Meireles, P. Aimar, P. Carvin, Analysing flux decline in dead-end filtration, Chem. Eng. Res. Des. 86 (2008) 1281–1293.
[14] P. Aimar, P. Bacchin, Slow colloidal aggregation and membrane fouling, J. Membr. Sci. 360 (2010) 70–76.
[15] D. Jassby, S.R. Chae, Z. Hendren, M. Wiesner, Membrane filtration of fullerene nanoparticle suspensions: effects of derivatization, pressure, electrolyte species and concentration, J. Colloid Interface Sci. 346 (2010) 296–302.
[16] T. Yin, H.W. Walker, D. Chen, Q. Yang, Influence of pH and ionic strength on the deposition of silver nanoparticles on microfiltration membranes, J. Membr. Sci. 449 (2014) 9–14.
[17] J. Labille, J. Brant, Stability of nanoparticles in water, Nanomedicine 5 (2010) 985–998.
[18] Y. Liang, N. Hilal, P. Langston, V. Starov, Interaction forces between colloidal particles in liquid: theory and experiment, Adv. Colloid Interface Sci. 134–135 (2007) 151–166.
[19] A.H. Taheri, L.N. Sim, C.T. Haur, E. Akhondi, A.G. Fane, The fouling potential of colloidal silica and humic acid and their mixtures, J. Membr. Sci. 433 (2013) 112–120.
[20] A.I. Schäfer, U. Schwicker, M.M. Fischer, A.G. Fane, T.D. Waite, Microfiltration of colloids and natural organic matter, J. Membr. Sci. 171 (2000) 151–172.
[21] A.S. Kim, A.E. Contreras, Q. Li, R. Yuan, Fundamental mechanisms of three-component combined fouling with experimental verification, Langmuir 25 (2009) 7815–7827.
[22] X. Shi, R. Field, N. Hankins, Review of fouling by mixed feeds in membrane filtration applied to water purification, Desalin. Water Treat. 35 (2011) 68–81.
[23] K.L. Chen, M. Elimelech, Influence of humic acid on the aggregation kinetics of fullerene (C60) nanoparticles in monovalent and divalent electrolyte solutions, J. Colloid Interface Sci. 309 (2007) 126–134.
[24] Y. Chen, H. Kim, Monte Carlo simulation of pore blocking and cake formation by interfacial interactions during membrane filtration, Desalination 233 (2008) 258–266.
[25] M. Wessling, Two-dimensional stochastic modeling of membrane fouling, Sep. Purif. Technol. 24 (2001) 375–387.
[26] A.E. Contreras, A. Kim, Q. Li, Combined fouling of nanofiltration membranes: mechanisms and effect of organic matter, J. Membr. Sci. 327 (2009) 87–95.
[27] D. Jermann, W. Pronk, R. Kagi, M. Halbeisen, M. Boller, Influence of interactions between NOM and particles on UF fouling mechanisms, Water Res. 42 (2008) 3870–3878.
[28] D. Jermann, W. Pronk, M. Boller, Mutual influences between natural organic matter and inorganic particles and their combined effect on ultrafiltration membrane fouling, Environ. Sci. Technol. 42 (2008) 9129–9136.
[29] S. Lin, Y. Cheng, J. Liu, M.R. Wiesner, Polymeric coatings on silver nanoparticles hinder autoaggregation but enhance attachment to uncoated surfaces, Langmuir 28 (2012) 4178–4186.
[30] J. Swenson, M.V. Smalley, H.L.M. Hatharasinghe, Mechanism and strength of polymer bridging flocculation, Phys. Rev. Lett. 81 (1998) 5840–5843.
[31] K. Mühle, Particle adhesion in coagulation and bridging flocculation, Colloid Polym. Sci. 263 (1985) 660–672.
[32] J.M.H.M. Scheutjens, G.J. Fleer, Statistical theory of the adsorption of interacting chain molecules. 2. Train, loop, and tail size distribution, J. Phys. Chem. 84 (1980) 178–190.
[33] G.P. van der Beek, M.A. Cohen Stuart, Polymer adsorption and desorption studies via $^1$H NMR relexation of the solvents, Langmuir 7 (1991) 327–334.
[34] B. Cattoz, T. Cosgrove, M. Crossman, S.W. Prescott, Surfactant-mediated desorption of polymer from the nanoparticle interface, Langmuir 28 (2012) 2485–2492.
[35] J.C. Dijt, M.A. Cohen Stuart, G.J. Fleer, Reflactometry as a tool for adsorption studies, Adv. Colloid Interface Sci. 50 (1994) 79–101.
[36] W.M. de Vos, B. Cattoz, M.P. Avery, T. Cosgrove, S.W. Prescott, Adsorption and surfactant-mediated desorption of poly(vinylpyrrolidone) on plasma- and piranha-cleaned silica surfaces, Langmuir 30 (2014) 8425–8431.
[37] W. van de Ven, I. Pünt, A. Kemperman, M. Wessling, Unraveling ultrafiltration of polysaccharides with flow field flow fractionation, J. Membr. Sci. 338 (2009) 67–74.
[38] C.O. Metin, L.W. Lake, C.R. Miranda, Q.P. Nguyen, Stability of aqueous silica nanoparticle dispersions, J. Nanopart. Res. 13 (2010) 839–850.
[39] J.K. Armstrong, R.B. Wenby, H.J. Meiselman, T.C. Fisher, The hydrodynamic radii of macromolecules and their effect on red blood cell aggregation, Biophys J. 87 (2004) 4259–4270.
[40] S. Robinson, P.A. Williams, Inhibition of protein adsorption onto silica by polyvinylpyrrolidone, Langmuir 18 (2002) 8743–8748.
[41] M.A. Cohen Stuart, Adsorbed polymers in colloidal systems: from statics to dynamics, Polym. J. 23 (1991) 669–682.
[42] R.M. McDonogh, A.G. Fane, C.J.D. Fell, H.-C. Flemming, The influence of polydispersity on the hydraulic behaviour of colloidal fouling layers on membranes Perturbations on the behaviour of the “ideal” colloidal layer, Colloids Surf. A 138 (1998) 231–244.
[43] J.A. Kitchener, Principles of action of polymeric flocculants, Br. Polym. J. 4 (1972) 217–229.
[44] A.S. Kim, E.M.V. Hoek, Cake structure in dead-end membrane filtration: Monte Carlo Simulations, Environ. Eng. Sci. 19 (2002) 373–386.